

Thermal maps of gases in heterogeneous reactions

Nanette N. Jarenwattananon¹, Stefan Glöggler¹, Trenton Otto¹, Arek Melkonian¹, William Morris†¹, Scott R. Burt², Omar M. Yaghi^{1,3,4,5} & Louis-S. Bouchard^{1,6,7}

More than 85 per cent of all chemical industry products are made using catalysts^{1,2}, the overwhelming majority of which are heterogeneous catalysts² that function at the gas–solid interface³. Consequently, much effort is invested in optimizing the design of catalytic reactors, usually by modelling⁴ the coupling between heat transfer, fluid dynamics and surface reaction kinetics. The complexity involved requires a calibration of model approximations against experimental observations^{5,6}, with temperature maps being particularly valuable because temperature control is often essential for optimal operation and because temperature gradients contain information about the energetics of a reaction. However, it is challenging to probe the behaviour of a gas inside a reactor without disturbing its flow, particularly when trying also to map the physical parameters and gradients that dictate heat and mass flow and catalytic efficiency^{1–9}. Although optical techniques^{10–12} and sensors^{13,14} have been used for that purpose, the former perform poorly in opaque media and the latter perturb the flow. NMR thermometry can measure temperature non-invasively, but traditional approaches applied to gases produce signals that depend only weakly on temperature^{15,16} are rapidly attenuated by diffusion^{16,17} or require contrast agents¹⁸ that may interfere with reactions. Here we present a new NMR thermometry technique that circumvents these problems by exploiting the inverse relationship between NMR linewidths and temperature caused by motional averaging in a weak magnetic field gradient. We demonstrate the concept by non-invasively mapping gas temperatures during the hydrogenation of propylene in reactors packed with metal nanoparticles and metal–organic framework catalysts, with measurement errors of less than four per cent of the absolute temperature. These results establish our technique as a non-invasive tool for locating hot and cold spots in catalyst-packed gas–solid reactors, with unprecedented capabilities for testing the approximations used in reactor modelling.

Figure 1 summarizes our technique, which exploits the effect of motional averaging in a weak magnetic field gradient ($\ll 1 \text{ G cm}^{-1}$). Nuclear spins acquire a random phase shift owing to the stochastic trajectories of molecules in the presence of a magnetic field gradient. This dephasing leads to faster signal decay, and spectral peaks are consequently broadened. Higher temperatures accelerate molecular motion¹⁹, leading to more efficient temporal averaging of the applied gradient (Fig. 1a). This method is a powerful complement to existing techniques for visualizing catalytic reactions under a range of experimental conditions^{7,8,20–27}.

The pulse sequence separates the phase-encoding scheme from the detection period to yield spectroscopic images (Supplementary Information). We apply a constant magnetic field gradient during the detection period to introduce temperature-dependent line broadening. This gradient differs from a conventional frequency-encoding gradient or pulsed-field-gradient NMR¹⁶ because it is much too weak to provide spatial encoding of the image or signal attenuation, respectively. When imaging gradients are used, Fourier transformation of the data set with respect to reciprocal space of the phase-encoding scheme yields an

image containing a one-dimensional NMR spectrum in each voxel. The linewidth variations in each voxel are converted into temperatures using the calibration described below.

We tested this method over a temperature range of 293–443 K using a catalyst-packed, laboratory-scale demonstration reactor in which propylene and hydrogen reacted to form propane (Methods). The dependence of linewidth on temperature was calibrated over the entire reactor by omitting phase-encoding gradients and comparing the observed linewidth against temperatures measured by fibre-optic temperature sensors. To get absolute temperatures, the temperature scale must be fixed by placing a sensor at a convenient location where perturbation of the flow is minimal (for example, near an inlet or outlet). In the absence of an applied gradient, measured linewidths in the chemical reactor system (Fig. 2) show negligible temperature dependence (Fig. 1b); internal magnetic field inhomogeneities are thus too weak to produce any significant effects. The situation changes when we apply a gradient to deliberately

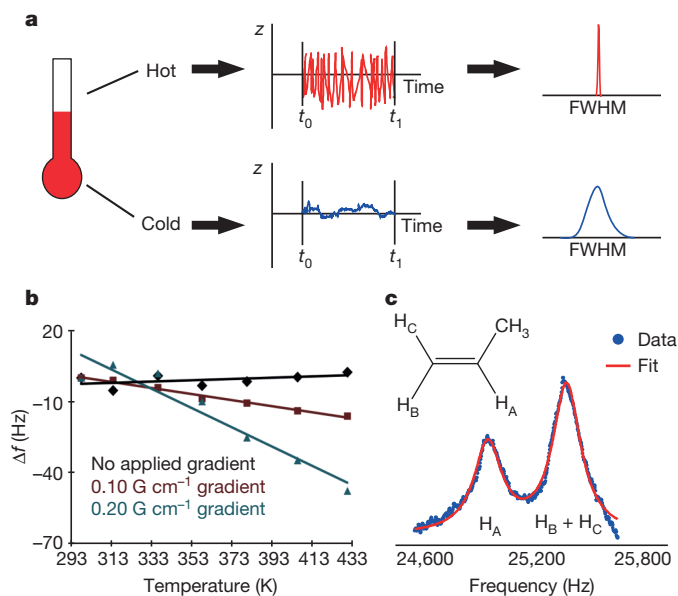


Figure 1 | Temperature mapping by motional averaging. **a**, At higher temperatures, gas molecules move faster and molecular motion averages the effects of the dephasing gradient. Because the spins experience more of the average magnetic field, linewidths are narrower. FWHM, full-width at half-maximum. **b**, Without a gradient, the linewidth is weakly dependent on temperature. As we turn on the external gradient, the linewidth dependence on temperature grows and becomes independent of the nature of the porous medium. **c**, In the calibration experiment of **b**, we fit the propylene spectrum at each temperature to a sum of Lorentzian distributions to extract the linewidth. Temperature calibrations were performed for over 30 different systems. The particular data shown in **b** is an example of one system.

¹Department of Chemistry and Biochemistry, University of California at Los Angeles, 607 Charles E. Young Drive East, Los Angeles, California 90095-1569, USA. ²Department of Chemistry and Biochemistry, Brigham Young University, C100 Benson Science Building, Provo, Utah 84602, USA. ³Department of Chemistry, University of California at Berkeley, 419 Latimer Hall, Berkeley, California 94720-1460, USA. ⁴Materials Sciences Division, Lawrence Berkeley National Laboratory, 1 Cyclotron Road, MS 66R00200, Berkeley, California 94720, USA. ⁵NanoCentury KAIST Institute and Graduate School of Energy, Environment, Water, and Sustainability (World Class University), 291 Daehak-ro (373-1 Guseong-dong), Yuseong-gu, Daejeon 305-701, South Korea. ⁶California NanoSystems Institute at UCLA, 570 Westwood Plaza, Building 114, Los Angeles, California 90095, USA. ⁷Department of Bioengineering, University of California at Los Angeles, 607 Charles E. Young Drive East, Los Angeles, California 90095-1569, USA. †Present address: Department of Chemistry, Northwestern University, 2145 Sheridan Road, Tech Institute, K-156, Evanston, Illinois 60208, USA.

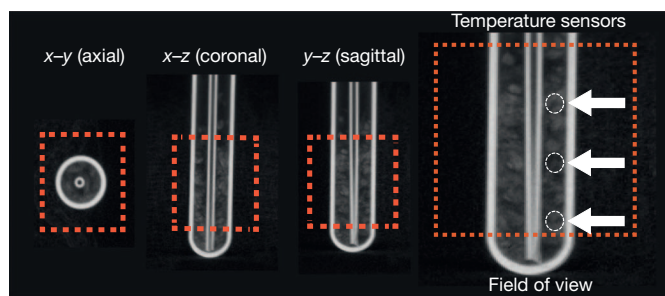


Figure 2 | The chemical reactor system. Orthogonal slices of the system determined by micro-computed tomography. The reactor shown here consists of a 10-mm Pyrex NMR tube, a gas inlet tube and a heterogeneous catalyst loaded on glass wool. To validate the NMR method, independent temperature measurements were made using fibre-optic probes placed at three different locations (arrows) within the NMR field of view (FOV). The approximate location of the FOV is indicated by the dashed box. The axial, coronal and sagittal planes correspond to those in Fig. 3.

broaden the lines (Fig. 1c), with a modest gradient (0.10 G cm^{-1}) yielding a temperature dependence of $-0.130 \pm 0.006 \text{ Hz K}^{-1}$ (Fig. 1b). Stronger gradients lead to stronger temperature dependence (Fig. 1b). The temperature dependence over this temperature range is well modelled by a linear regression.

Figure 3 depicts thermal maps of two reactors, each packed with a different catalyst: Pt nanoparticles (PtNP) or a multivariate metal-organic framework metallated with Pd (Pd-MOF) supported on glass wool. For the PtNP reactor system, a magnetic field gradient of 0.05 G cm^{-1} causes the propylene linewidth to have the form

$$\Delta f \text{ (Hz)} = [-0.16 \pm 0.01 \text{ Hz K}^{-1}]T \text{ (K)} + [151 \pm 1 \text{ Hz}] \quad (1)$$

where T is temperature. For the Pd-MOF system and an identical gradient, the linewidth is

$$\Delta f \text{ (Hz)} = [-0.10 \pm 0.01 \text{ Hz K}^{-1}]T \text{ (K)} + [119 \pm 1 \text{ Hz}] \quad (2)$$

The slopes of the lines described by equations (1) and (2), which encode the temperature dependences of the linewidths, together with the point-sensor readout reference, yield absolute temperature maps for the PtNP and Pd-MOF reactor beds, respectively. Figure 3 shows the thermal images for axial, sagittal, and coronal views in which only pixels with a signal-to-noise ratio (SNR) greater than four are displayed. These images show significant temperature variations throughout the catalyst bed, as expected for a heterogeneous reactor. The temperature inhomogeneities correlate with both the packing of the catalyst-impregnated glass wool (Fig. 3) and also the placement of the inlet and the outlet of the reactor. Owing to non-uniform catalyst packing, some regions are more active than others, leading to differences in catalytic conversion ('hot spots' and 'cold spots'). Another application of such thermal maps, if the heat capacity of the medium is known, would be to map spatial gradients in the internal energy (U) of the reaction through the thermodynamic relationship $\Delta U = C_V \Delta T$. From these, we could derive a fundamental thermodynamic quantity, ΔU , of the reaction, which reveals the flow of energy. The effective heat capacity of the medium (C_V) could potentially be inferred from microcomputed tomography images such as those of Fig. 2. The characteristic length scales of $|\Delta T|$ could be compared with those of the microcomputed tomography map in similar reactors to gain insight into the thermal flux of the system (Supplementary Information).

To validate the NMR-derived temperature measurements, three fibre-optic temperature sensors were placed at the centre of the FOV, and 4 mm below and 4 mm above the FOV centre (Fig. 3). The sensors in the PtNP reactor measured temperatures of 398, 412 and 427 K, which correspond well to the NMR-derived temperatures in the coronal map (that is, 400, 417 and 424 K). Similarly, the *in situ* temperature measurements in the Pd-MOF reactor gave 382, 411 and 425 K, which compare well with the NMR-derived measurements in the sagittal map (that is, 389, 416 and 441 K). The random error in the NMR-derived temperature measurement

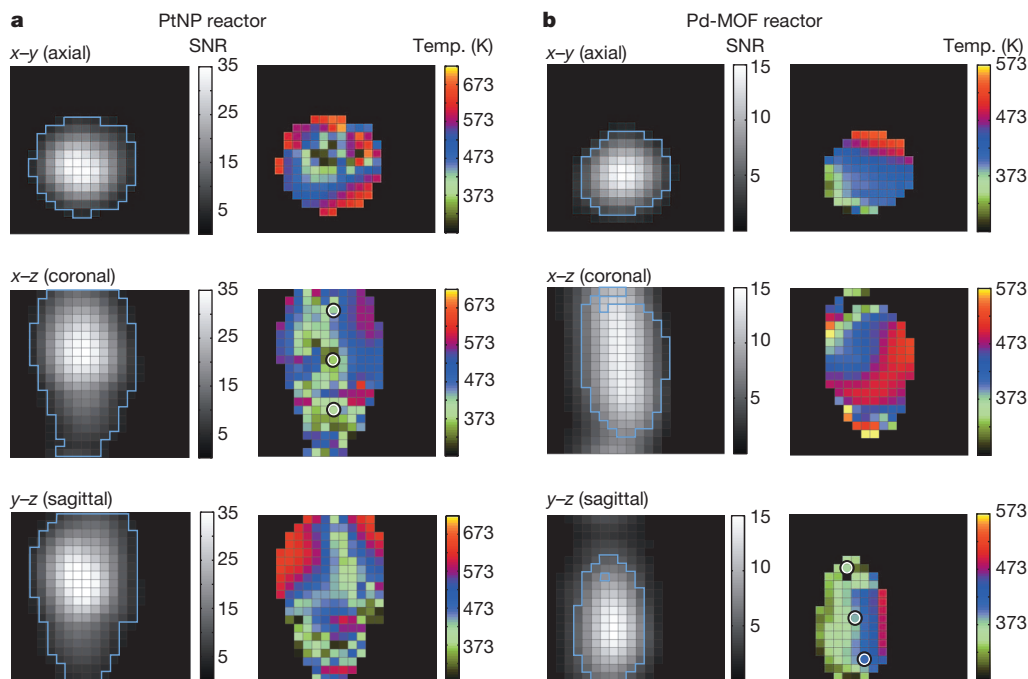


Figure 3 | Temperature mapping. a, b, Two-dimensional NMR signal-to-noise ratio (SNR) maps (greyscale) and corresponding gas-phase thermal maps (colour) of one reactor packed with 10-mm PtNP (a) and another packed with Pd-MOF (b). SNR maps detail the signal intensity of proton resonances used to derive the temperature. Each pixel corresponds to an in-plane, $0.73 \text{ mm} \times 0.73 \text{ mm}$ region and is assigned a linewidth-based temperature.

Temperature was calculated only for pixels with $\text{SNR} > 4$ (blue outline). The temperature measurement was confirmed by fibre-optic temperature sensors placed within the FOV, indicated by circles on the thermal maps. Sensor probe alignment relative to the reactor is shown in Fig. 2. Thermal maps were generated for more than 15 experiments. The particular thermal maps shown above are two representative examples of those maps.

$$\frac{\delta T}{T} = \sqrt{\left(\frac{\delta(\Delta f)}{\Delta f}\right)^2 + \left(\frac{\delta(\Delta f/\Delta T)}{\Delta f/\Delta T}\right)^2}$$

was calculated to be 4% on the Kelvin scale using the relative errors in the linear regression, $\delta(\Delta f)/\Delta f$ and $\delta(\Delta f/\Delta T)/(\Delta f/\Delta T)$, where Δf is the linewidth from the fit of the spectrum and $\Delta f/\Delta T$ is the slope of the temperature calibration curve. The disagreement between NMR-derived temperatures and fibre-optic-sensor measurements was at most 4%; thus, systematic errors for the systems studied were not significant. The correspondence of these results demonstrates the ability to map temperatures of reacting gases inside an operating catalytic reactor with millimetre resolution using the NMR signal from thermally polarized protons.

The above proof-of-principle experiments used a 10-mm reactor; so 1-mm-diameter point sensors are much smaller than the reactor and thus cause minimal perturbation of the flow. Once validated, the method can be used on smaller reactors with only a single reference temperature measured at a convenient location outside the reactor bed to avoid perturbing the flow. Thermal maps of a microreactor are shown in Fig. 4, where para-state-enriched hydrogen^{22–27} was used as reactant to overcome the loss of signal associated with the smaller image voxels. This reactor was packed without glass wool support.

NMR thermometry based on the nuclear spin–lattice relaxation time (T_1) or spin–spin relaxation time (T_2) is widely applicable in liquids, but either impractical or insensitive when applied to gas-phase reactions: T_2 measured over the temperature range 303–413 K (Methods) lacked a statistically significant temperature dependence, and inversion-recovery measurements showed that T_1 is temperature dependent ($-2.3 \pm 0.2 \text{ ms K}^{-1}$) but required a minimum of 51 inversion times to yield temperature measurements with comparable precision (equating to a scan time of 1,000 h to create thermal maps). If the number of inversion-recovery steps is reduced to four, the error in temperature would be a factor of forty greater than with our motional-averaging technique and

the scan time would still be a factor of five times longer ($\sim 2.5 \text{ h}$) than our technique ($\sim 30 \text{ min}$).

We expect our motional-averaging NMR method, which outperforms existing thermometry techniques in the gas phase, to open the way to studies of *in situ* thermodynamics and optimization of gas–solid reactors. The method is robust relative to factors such as pressure, gas composition, reactor type, catalyst type, reaction rate and steady-state conversion (Supplementary Information). Moreover, its temperature sensitivity is tunable: the stronger the applied gradient, the stronger the dependence on temperature and the higher the sensitivity of the method. In practice, the gradient should be significantly stronger than the internal magnetic field inhomogeneities to ensure that the temperature calibration coefficient is essentially sample independent, but it should be weak enough to avoid broadening the lines beyond detection. And because the primary requirement is the presence of NMR-active nuclei in a gas-phase component, the technique will be applicable to most industrially relevant reactions (including those involving mixed gas–liquid–solid phases).

METHODS SUMMARY

NMR spectroscopy and imaging were performed using a Varian 9.4 T VNMRs 400 MHz magnet with air-regulated variable temperature control and micro-imaging gradients. Samples were allowed to equilibrate thermally for 10 min at each temperature, and this was followed by probe retuning. The temperature calibration was performed using FISO FOT-L fibre-optic temperature sensors (FISO Technologies, Inc.). Propylene and hydrogen gases (ultrahigh purity) were obtained from Airgas. Data was processed using VNMRJ 2.3 A and MATLAB (MathWorks).

The catalysts were prepared following reported procedures^{27–30}. Details about the motional-averaging technique calibration, temperature mapping, T_1 and T_2 relaxation, and microreactor imaging³⁰ can be found in the online Methods section.

Online Content Any additional Methods, Extended Data display items and Source Data are available in the online version of the paper; references unique to these sections appear only in the online paper.

Received 23 April 2012; accepted 23 July 2013.

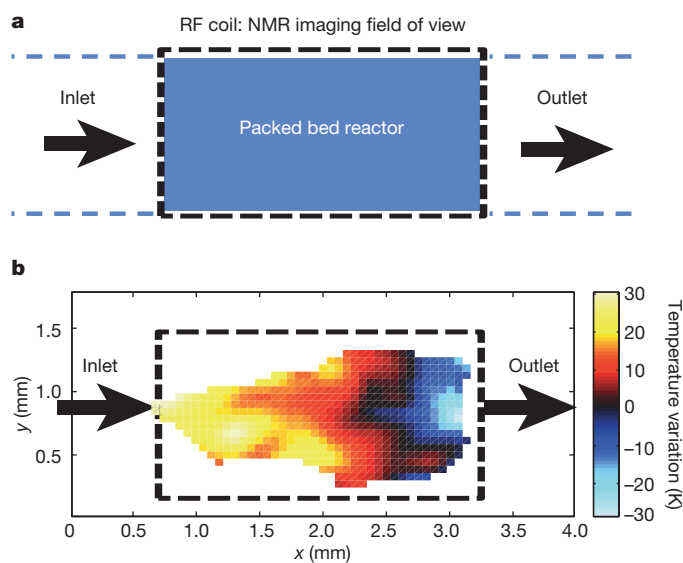


Figure 4 | Thermal map of gases in an operating catalytic microreactor. Signal enhancement from para-state hydrogen was used to provide detailed views inside the microreactor, which was held at approximately 418 K by using a variable temperature controller to preheat the gas flowing through a heat exchange radio-frequency (RF) coil. **a**, Schematic view; **b**, thermal map. The temperature calibration coefficient was $-0.200 \pm 0.006 \text{ Hz K}^{-1}$. The thermal map depicts temperature changes relative to the incoming gas. Spatial distributions of linewidths were mapped on five different reactors prepared similarly. Each reactor exhibited comparable heterogeneity in the temperature distributions.

- Hagen, J. *Industrial Catalysis: A Practical Approach 2* (2nd edn, Wiley-VCH, 2006).
- Chorkendorff, I. & Niemantsverdriet, J. W. *Concepts of Modern Catalysis and Kinetics 11* (2nd edn, Wiley-VCH, 2007).
- Rothenberg, G. *Catalysis: Concepts and Green Applications 129* (1st edn, Wiley-VCH, 2008).
- Schwiadernoch, R., Tischer, S., Deutschmann, O. & Warnatz, J. Experimental and numerical investigation of the ignition of methane combustion in a platinum-coated honeycomb monolith. *Proc. Combust. Inst.* **29**, 1005–1011 (2002).
- Buurmans, I. L. C. *et al.* Catalytic activity in individual cracking catalyst particles imaged throughout different life stages by selective staining. *Nature Chem.* **3**, 862–867 (2011).
- de Smit, E. *et al.* Nanoscale chemical imaging of a working catalyst by scanning transmission X-ray microscopy. *Nature* **456**, 222–225 (2008).
- Gladden, L. F. Applications of *in situ* magnetic resonance techniques in chemical reaction engineering. *Top. Catal.* **8**, 87–95 (1999).
- Lysova, A. A. & Koptuyug, I. V. Magnetic resonance imaging methods for *in situ* studies in heterogeneous catalysis. *Chem. Soc. Rev.* **39**, 4585–4601 (2010).
- Horn, R. *et al.* Reactor for *in-situ* measurements of spatially resolved kinetic data in heterogeneous catalysis. *Rev. Sci. Instrum.* **81**, 064102 (2010).
- Taylor, S. J. & Morken, J. P. Thermographic selection of effective catalysts from an encoded polymer-boundary library. *Science* **280**, 267–270 (1998).
- Urakawa, A. & Baiker, A. Space-resolved profiling relevant in heterogeneous catalysis. *Top. Catal.* **52**, 1312–1322 (2009).
- Korup, O., Mavlyankariev, S., Geske, M., Goldsmith, C. F. & Horn, R. Measurement and analysis of spatial reactor profiles in high temperature catalysis research. *Chem. Eng. Process.* **50**, 998–1009 (2011).
- Dietrich, T. R. *Microchemical Engineering in Practice* 199–239 (Top. Appl. Phys. 10, Wiley, 2009).
- Jensen, K. F. *et al.* in *Microreaction Technology* (ed. Ehrfeld, W.) 2–9 (Springer, 1997).
- Beckmann, P. A. & Dybowski, C. A thermometer for non-spinning solid state NMR spectroscopy. *J. Magn. Reson.* **146**, 379–380 (2000).
- Callaghan, P. T. *Principles of Nuclear Magnetic Resonance Microscopy* 59–69 328–419 (Oxford Univ. Press, 1994).
- Galiana, G., Branca, R. T., Jenista, E. R. & Warren, W. S. Accurate temperature imaging based on intermolecular coherences in magnetic resonance. *Science* **322**, 421–424 (2008).
- Webb, A. G. Temperature measurements using NMR. *Ann. Rep. NMR Spectrosc.* **45**, 1–67 (2002).

19. Cussler, E. L. *Diffusion: Mass Transfer in Fluid Systems* 13–45 (Cambridge Univ. Press, 1997).
20. Ferstl, W. *et al.* Inline analysis in microreaction technology: a suitable tool for process screening and optimization. *Chem. Eng. Technol.* **30**, 370–378 (2007).
21. Bouchard, L. S. *et al.* NMR imaging of catalytic hydrogenation in microreactors with the use of parahydrogen. *Science* **319**, 442–445 (2008).
22. Adams, R. W. *et al.* Reversible interactions with para-hydrogen enhance NMR sensitivity by polarization transfer. *Science* **323**, 1708–1711 (2009).
23. Bowers, C. R. & Weitekamp, D. P. Parahydrogen and synthesis allow dramatically enhanced nuclear alignment. *J. Am. Chem. Soc.* **109**, 5541–5542 (1987).
24. Eisenschmid, J. *et al.* Para hydrogen induced polarization in hydrogenation reactions. *J. Am. Chem. Soc.* **109**, 8089–8091 (1987).
25. Duckett, S. B. & Wood, N. J. Parahydrogen-based NMR methods as a mechanistic probe in inorganic chemistry. *Coord. Chem. Rev.* **252**, 2278–2291 (2008).
26. Kovtunov, K. V., Beck, I. E., Bukhtiyarov, V. I. & Koptyug, I. V. Observation of parahydrogen-induced polarization in heterogeneous hydrogenation on supported metal catalysts. *Angew. Chem. Int. Ed.* **47**, 1492–1495 (2008).
27. Sharma, R. & Bouchard, L. S. Strongly hyperpolarized gas from parahydrogen by rational design of ligand-capped nanoparticles. *Sci. Rep.* **2**, 277–281 (2012).
28. Deng, H. *et al.* Multiple functional groups of varying ratios in metal-organic frameworks. *Science* **327**, 846–850 (2010).
29. Doonan, C. J., Morris, W., Furukawa, H. & Yaghi, O. M. Isoreticular metalation of metal-organic frameworks. *J. Am. Chem. Soc.* **131**, 9492–9493 (2009).
30. Burt, S. R. *MRI of Heterogeneous Hydrogenation Reactions Using Parahydrogen Polarization* 37–39, 69–100. PhD thesis, Univ. California, Berkeley (2008).

Supplementary Information is available in the online version of the paper.

Acknowledgements We thank J. Reimer, C. T. Campbell, W. S. Warren, I. Oppenheim and R. Bruinsma for discussions; N. K. Garg, C. T. Campbell, W. Gelbart and C. Knobler for reading the manuscript; M. T. Yeung for technical help with MATLAB; and J. Brown and R. Sharma for assistance with chemical synthesis. This work was funded by a Dreyfus New Faculty Award (L.-S.B.); a Beckman Young Investigator Award (L.-S.B.); US NSF CHE-1153159 (L.-S.B., O.M.Y.); BASF, Germany (synthesis); and the US DOE (O.M.Y.; porosity measurements).

Author Contributions N.N.J., S.G., T.O., A.M. and S.R.B. performed the experiments and collected the data. N.N.J. and W.M. performed the chemical synthesis. N.N.J., S.G., T.O., A.M., S.R.B. and L.-S.B. conducted the data processing and error analysis. N.N.J., S.G., S.R.B., O.M.Y. and L.-S.B. wrote the paper. All authors discussed the results and commented on the manuscript.

Author Information Reprints and permissions information is available at www.nature.com/reprints. The authors declare no competing financial interests. Readers are welcome to comment on the online version of the paper. Correspondence and requests for materials should be addressed to L.-S.B. (bouchard@chem.ucla.edu).

METHODS

PtNP catalyst preparation. The synthesis of PtNP follows the reported protocols²⁷. The supported heterogeneous catalyst used in reaction imaging was made by soaking a piece of glass wool (SiO₂) in an aqueous dispersion of *p*-mercaptobenzoic-capped, 2.5 ± 0.4 nm PtNP to yield 1-wt% Pt/SiO₂.

Pd-MOF catalyst preparation. MTV-MOF-AB was prepared in accordance with reported procedures²⁸. The free amine (-NH₂) was metallated with palladium by post-modification to give Pd-MOF (ref. 29). The Pd-MOF catalyst was then mixed with TiO₂ nanopowder and packed with glass wool to obtain the supported heterogeneous catalyst used in reaction imaging.

Calibration of motional-averaging technique. A 10-mm NMR tube was packed with catalyst-loaded glass wool. For flowing propylene gas (40 p.s.i., 15 cc min⁻¹), an FID was acquired between 303 and 413 K in steps of 10 K. A spin-echo pulse sequence was used, and a magnetic field gradient was applied during acquisition. Spectral windows were fitted to a sum of Lorentzian curves with MATLAB, using nonlinear least-squares regression. The temperature reported is that of the gaseous component contributing to the NMR signal, which is in local equilibrium with the solid phase (Supplementary Information).

Temperature mapping. Propylene gas (40 p.s.i., 15 cc min⁻¹) and para-state hydrogen gas (40 p.s.i., 15 cc min⁻¹) were flowed through the system. Each image was acquired using a spin-echo imaging pulse sequence with 441 transients during a continuous flow reaction for a total acquisition time of 33 min. The scan time, during which images are made from a steady-state flow, could be further reduced by compressed sensing. The spectrum of each pixel with SNR > 4 was analysed in

MATLAB, using nonlinear least-squares regression to fit the propane and propylene resonances to a sum of Lorentzian curves. The reactors we investigated featured voxel linewidths in the range 40–300 Hz, depending on the catalyst type and support. The temperature measurement was confirmed using a FISO FOT-L sensor. The spatial resolution of the experiment is limited by the SNR of the image, as in conventional MRI experiments. For higher spatial resolutions (smaller voxels), the applied gradient can be even weaker. This is because the gradient needs to be only about 5–10 times larger than the linewidth over the voxel in the absence of a gradient.

T₁ relaxometry. A 10-mm NMR tube with a J. Young valve adaptor was pressurized to 15 p.s.i. with propylene gas. An inversion-recovery pulse sequence with 51 inversion times was applied, and relaxation time was determined by fitting the data to a nonlinear least-squares exponential recovery curve in MATLAB. T₁ was determined between 303 and 413 K in steps of 10 K.

T₂ relaxometry. A 10-mm NMR tube with a J. Young valve adaptor was pressurized to 15 p.s.i. with propylene gas. A single-shot Carr–Purcell–Meiboom–Gill echo train of 100 echoes was applied for interpulse spacing between 1 and 20 ms. Relaxation time was determined by fitting the amplitude of alternating echoes to a nonlinear least-squares exponential decay curve in MATLAB. T₂ was determined between 303 and 413 K in steps of 10 K.

Microreactor imaging. The catalyst, Wilkinson's catalyst supported on silica gel, and the microreactor were prepared as described in ref. 30. Polarization induced by para-state hydrogen (mixture contains hydrogen enriched to 50% para-state hydrogen), was used to provide signal enhancement from the microreaction. The calibration and data analysis were similar to that described above.